Atmos. Chem. Phys. Discuss., 7, 4857–4888, 2007
www.atmos-chem-phys-discuss.net/7/4857/2007/

Atmospheric Chemistry and Physics Discussions

Global distributions of water vapour isotopologues retrieved from IMG/ADEOS data

H. Herbin[1], D. Hurtmans[1], S. Turquety[2], C. Wespes[1], B. Barret[1,*], J. Hadji-Lazaro[2], C. Clerbaux[1,2], and P.-F. Coheur[1,]**

[1]Spectroscopie de l'Atmosphère, Service de Chimie Quantique et de Photophysique, Université Libre de Bruxelles (U.L.B.), Brussels, Belgium
[2]Service d'Aéronomie/IPSL, CNRS, Université Pierre et Marie Curie, Paris, France
[*]now at: Laboratoire d'Aérologie, UMR 5560 CNRS/Université Paul Sabatier, Observatoire de Midi-Pyrénées, Toulouse, France
[**]Research Associate with the F.N.R.S, Belgium

Received: 28 February 2007 – Accepted: 19 March 2007 – Published: 5 April 2007

Correspondence to: H. Herbin (hherbin@ulb.ac.be)

Abstract

The analysis of the atmospheric isotopologic water vapour composition provides valuable information on many climate, chemical and atmospheric circulation processes. The remote-sensing of the water isotopologues remains a challenge, which is enhanced by the large and fast variations of their spatial distributions. This paper presents for the first time the simultaneous retrieval of global distributions of the main water isotopologues (i.e. $H_2^{16}O$, $H_2^{18}O$, HOD) and their ratios. The results are obtained by exploiting the high resolution infrared spectra recorded by the Interferometric Monitor for Greenhouse gases (IMG) instrument, which operated in the nadir geometry onboard the ADEOS satellite between 1996 and 1997. The retrievals are performed on a series of cloud-free radiance measurements in two atmospheric windows (1205–1228 cm^{-1}; 2004–2032 cm^{-1}) using a line-by-line radiative transfer model and an inversion procedure based on the Optimal Estimation Method (OEM). Characterizations in terms of vertical sensitivity and error budget are provided. A relatively high vertical resolution is achieved for $H_2^{16}O$ (~4–5 km), and we show that the retrieved profiles are in good agreement with local sonde measurements, representative of different latitudes. The retrieved global distributions of $H_2^{16}O$, $H_2^{18}O$, HOD and their ratios are also found to be consistent with previous experimental studies and models. The ocean-earth difference, the latitudinal and vertical dependence of the water vapour amount and the isotopologic depletion are notably well reproduced. Others trends, possibly related to smaller scales variations in the vertical profiles are also discussed. Despite the difficulties encountered for computing accurately the isotopologic ratios, our results demonstrate the ability of the infrared nadir sounding for monitoring atmospheric isotopologic water vapour distributions on a global scale.

ACPD

7, 4857–4888, 2007

1 Introduction

Water vapour is involved in many key atmospheric processes including radiation transfer, circulation dynamics, homogeneous and heterogeneous chemistry (Solomon, 1999; Coffey et al., 2006). The study of atmospheric water vapour has further gained interest since the discovery of the increasing humidity over the last half century (Rosenlof et al., 2001; 2003), the causes of which are not yet fully understood (Kuang et al., 2003; McCarthy et al., 2004; Franz et al., 2005; Schmidt et al., 2005; Coffey et al., 2006). In the stratosphere, the amount of water vapour has a direct impact on the concentration of the OH radical, which plays an important role in catalytic cycles of ozone destruction, chlorine activation, denitrification and methane decomposition (Forster et al., 2002; Kirk-Davidoff et al., 1999; Tabazadeh et al., 2000; Shindell, 2001; McCarthy et al., 2004). In the troposphere, clouds, precipitations and the major role of gaseous water in the greenhouse effect, make this species a key compound of the global climate system (Schneider et al., 1999; Hartmann, 2002).

The study of the isotopologic composition of atmospheric water vapour is used to derive information on many stages of the water cycle (Bechtel et al., 2003). Measurements of stable isotopologues of water are currently used for many applications, including: paleoclimate (Masson-Delmotte et al., 2005; Jouzel et al., 1997), cloud physics (Webster et al., 2003), exchanges between the upper troposphere and the lower stratosphere (Kuang et al. 2003; Moyer et al., 1996) and climate studies (precipitations, storms, hurricanes) (Bowen et al., 2003; Ciais et al., 2004; Gedzelman et al., 2003; Smith, 1992; Lawrence et al., 2002). This is because isotopologic ratios of water strongly depend upon the evaporation conditions and the condensation history of the air mass during transport (Strong et al., 2007). The process is known as the Vapour Pressure Isotopologue Effect (VPIE): Heavier isotopologues (here HDO and $H_2^{18}O$) have lower vapour pressures than the lighter one ($H_2^{16}O$) and this leads to an isotopologic fractionation during changes of phase. Hence, when vapour phase and condensed phase are in thermodynamic equilibrium, the lighter isotopologues will con-

ACPD
7, 4857–4888, 2007

dense more slowly and will evaporate at a higher rate than the heavier ones, which in turn will tend to concentrate in the liquid or solid phase. The result of this VPIE is that the heavier isotopologic species of atmospheric water are progressively removed, in particular with altitude, and become depleted relative to the Standard Mean Ocean Water (SMOW) values.

An accurate knowledge of the concentration of the different water isotopologues and their vertical/horizontal evolution are of great interest for a better understanding of the processes controlling the water vapour budget (Bechtel et al., 2003). However, their quick changes of concentration in space and time, associated with the very important concentration decay with altitude is a difficulty for these studies, and few measured profiles of the heavier isotopologues of water vapour have been reported (Zahn et al., 2006, and references therein). The measurements from space-borne instruments, which are the only means for determining extended spatial distributions, are particularly sparse.

In previous works, the Atmospheric Trace Molecule Spectroscopy (ATMOS) instrument was used to measure $H_2^{16}O$, HDO and their ratio in the Upper Troposphere and Lower Stratosphere (UT/LS); it provided information mainly on transport in the tropical UT/LS (Moyer et al., 1996; Kuang et al., 2003). The Interferometric Monitor for Greenhouse gases (IMG) provided a latitudinal distribution of HDO around 4 km high (Zakharov et al., 2004). Finally, the Tropospheric Emission Spectrometer (TES) has recently enable deriving global distributions of the tropospheric HDO/ $H_2^{16}O$ ratio between 0 and 800 hPa (Worden et al., 2006 and 2007). In the latter study, the authors introduced a correlation between $H_2^{16}O$ and HOD values for the retrievals.

In this work, we intend to go further in probing the isotopologic composition of water vapour from satellite. The principal objective of this paper is to characterize the capabilities of high-spectral resolution infrared nadir sounder to provide simultaneous information on the vertical and zonal concentration distributions of three isotopologues ($H_2^{16}O$, $H_2^{18}O$ and HOD) and their ratio. For $H_2^{18}O$, these are the first attempts of retrievals in the nadir view. In contrast to the work of Worden et al. (2006 and 2007), the

retrievals are performed for each isotopologue independently from the others.

In the next section, the IMG instrument, the spectra and the retrieval method are briefly described. Section 3 presents the profiles of the different water isotopologues and their ratio for a small selection of IMG spectra coincident with water balloon-borne soundings. The comparison of the retrieved profiles with sonde data is discussed with respect to the measurement vertical sensitivity and error sources. Section 4 presents the distribution of the isotopologic species and ratios in partial columns between ground and 16 km of altitude on the global scale for the longest IMG operation period, corresponding to ten successive days in April 1997. In particular, the spatial variability of $HOD/H_2^{16}O$ and $H_2^{18}O/H_2^{16}O$ ratios are presented and discussed. Section 5 summarizes our results and puts forward some perspectives for future applications.

2 Measurements and methods

2.1 Measurements

The IMG instrument was launched onboard the ADEOS platform on August 1996 and ceased operating in June 1997 (Kobayashi et al., 1999). ADEOS was a sun-synchronous, ground-track repeat polar orbiting satellite at about 800 km altitude, providing a global Earth coverage in 4 days. The IMG instrument was a nadir-viewing Fourier transform interferometer that recorded the thermal infrared emission of the Earth-atmosphere system between 650 and 3000 cm^{-1}. Its maximum optical path difference was 10 cm, leading to a nominal spectral resolution of 0.1 cm^{-1}. The spectral range was covered by three separate spectral portions : two photovoltaic InSb detectors were used to record band 1 from 2300 to 3000 cm^{-1} and band 2 from 2000 to 2500 cm^{-1}, and a photoconductive type HgCdTe detector was used for band 3 from 600 to 2000 cm^{-1}. Each detector had a field of view corresponding to a 8 km×8 km footprint on the ground. The IMG spectra were recorded in batches of six successive measurements, separated by 86 km along the track, followed by reference blackbody

ACPD
7, 4857–4888, 2007

EGU

calibration measurements. The IMG operation mode was limited to periods of 4 successive days of measurement out of 10 days, except for a period of ten days from 1 to 10 of April 1997. Due to the very weak signal to noise ratio, the Band 1 has not been exploited up to now.

In this study, we use the spectra from the 1–10 April 1997 period, provided by bands 2 and 3. The vertical distributions are retrieved from the spectra using the Atmosphit software developed at the Université Libre de Bruxelles. This software is based on a detailed line-by-line radiative transfer model, including ray tracing for various geometries and a retrieval scheme that relies on the Optimal Estimation Method (OEM) (Rodgers, 2000). The theoretical elements relevant for the present study are similar to those described by (Barret et al., 2005 and Coheur et al., 2005). They are only briefly summarized hereafter.

2.2 Retrieval methodology

For an atmosphere divided in discrete layers, the forward radiative transfer equation gives an analytical relationship between the measured vector **y** (in our case, the radiance) and the true atmospheric state **x** (variables to be retrieved: surface temperature, vertical concentration profile, etc) and is written as:

$$\mathbf{y} = \mathbf{F}(\mathbf{x}; \mathbf{b}) + \varepsilon \quad (1)$$

where **F** is the forward radiative transfer function, **b** represents the fixed parameters affecting the measurement (atmospheric temperature, pressure, instrumental line shape (ILS), etc) and ε is the measurement noise.

A synthetic spectrum, approximation of **F**, is computed using the line parameters (positions, intensities, broadening, shifting and their temperature dependency) and absorption cross-sections compiled in spectroscopic databases, as well as the absorption continua from the MT-CKD model (Clough et al., 2005). The molecular absorption lines are computed using a Voigt line shape and the resulting spectrum is processed to account for the ILS contribution.

The retrieval method aims at determining the state vector **x** from the measurement vector **y**. For nadir-viewing satellites, however, the spectra are the result of an integrated view of the atmosphere. As a consequence, the retrieval of a vertically resolved profile from the measurement is mathematically ill conditioned, meaning that it has no unique solution. A meaningful solution can, however, be obtained by regularizing the retrieval with *a priori* information about the variables. This information is composed of an *a priori* profile $\mathbf{x}_a$ and an *a priori* variance-covariance matrix $\mathbf{S}_a$ (Rodgers, 2000). In this case, the goal of the inversion is to find $\hat{\mathbf{x}}$, which is the approximation of the true state **x**, which best agrees with both the measurement and the *a priori* information. $\hat{\mathbf{x}}$ is found by iterating:

$$\hat{\mathbf{x}}_{i+1} = \mathbf{x}_a + (\mathbf{K}_i^T \mathbf{S}_\varepsilon^{-1} \mathbf{K}_i + \mathbf{S}_a^{-1})^{-1} \mathbf{K}_i^T \mathbf{S}_\varepsilon^{-1} \left[\mathbf{y} - \mathbf{F}(\hat{\mathbf{x}}_i) + \mathbf{K}_i(\hat{\mathbf{x}}_i - \mathbf{x}_a)\right], \quad (2)$$

with **K** being the Jacobian matrix, the rows of which are the partial derivatives of the measurement with respect to the retrieved variables: $\mathbf{K}=\partial\mathbf{y}/\partial\mathbf{x}$. $\mathbf{S}_\varepsilon$ is the measured signal error variance-covariance matrix and is chosen to be diagonal with identical diagonal elements σ_ε^2($\mathbf{S}_\varepsilon = \sigma_\varepsilon^2\mathbf{I}$) (Barret et al., 2005; Coheur et al., 2005), where σ_ε is a constraint representing the noise equivalent spectral radiance. The retrieved state is obtained after convergence, when the absolute difference between every element of **F** modeled at two successive iteration steps, $|\mathbf{F}(\hat{\mathbf{x}}_{i+1}) - \mathbf{F}(\hat{\mathbf{x}}_i)|$, is less than a fraction (20%) of σ_ε.

The characterization of the retrieved quantities in terms of sensitivity and the error sources budget is essential to estimate the quality of the results. In the case of the linear approximation used here, the OEM provides an efficient way for characterizing the retrieved state, which is given by (Rodgers, 2000):

$$\hat{\mathbf{x}} = \mathbf{x}_a + \mathbf{A}(\mathbf{x} - \mathbf{x}_a) + \mathbf{G}(\varepsilon + \mathbf{K}_b(\mathbf{b} - \hat{\mathbf{b}})), \quad (3)$$

where $\hat{\mathbf{b}}$ is the approximate of the model parameters **b**, the Jacobian $\mathbf{K}_b = \partial\mathbf{F}/\partial\mathbf{b}$ characterizes the sensitivity of the forward model **F** to the model parameters. **G** is the gain matrix whose rows are the derivatives of the retrieved state with respect to the

ACPD
7, 4857–4888, 2007

spectral points and it is defined by:

$$\mathbf{G} = \partial\hat{\mathbf{x}}/\partial\mathbf{y} \tag{4}$$

A, the averaging kernel matrix, gives a measure of the sensitivity of the retrieved state to the true state. It is defined by:

$$\mathbf{A} = \partial\hat{\mathbf{x}}/\partial\mathbf{x} = \mathbf{GK} \tag{5}$$

At a given level, the peak of the averaging kernel rows gives the altitude of maximum sensitivity whereas its full width at half maximum is an estimate of the vertical resolution. The trace of **A**, known as the Degrees Of Freedom for Signal (DOFS), indicates the number of independent values of the state vector which can be retrieved from the measurements.

The global error can be inferred from Eq. (3) by considering the difference between the retrieved and the true state:

$$\hat{\mathbf{x}} - \mathbf{x} = (\mathbf{A} - \mathbf{I})(\mathbf{x} - \mathbf{x}_a) + \mathbf{G}\varepsilon + \mathbf{GK}_b(\mathbf{b} - \hat{\mathbf{b}}) \tag{6}$$

This Eq. (6) can be decomposed into three different contributions:

- $(\mathbf{A} - \mathbf{I})(\mathbf{x} - \mathbf{x}_a)$ is the smoothing error, which accounts for the vertical sensitivity of the measurements to the retrieved profile.
- $\mathbf{G}\varepsilon$ is the measurement error, associated to the spectral noise.
- $\mathbf{GK}_b(\mathbf{b} - \hat{\mathbf{b}})$ is the model parameters error, which represents the imperfect knowledge of the model parameters.

Their covariances matrices are respectively given by:

$$\mathbf{S}_{\text{smoothing}} = (\mathbf{A} - \mathbf{I})\mathbf{S}_a(\mathbf{A} - \mathbf{I})^T \tag{7}$$

$$\mathbf{S}_{\text{meas.}} = \mathbf{G}\mathbf{S}_\varepsilon\mathbf{G}^T \tag{8}$$

$$\mathbf{S}_{\text{mod.param.}} = \mathbf{GK}_b\mathbf{S}_b(\mathbf{GK}_b)^T \tag{9}$$

with $\mathbf{S}_b$ representing uncertainty on the forward model parameters (e.g. the temperature and the humidity profiles).

The total error variance-covariance matrix can then be regarded as the sum of these individual contributions:

$$\mathbf{S}_{\text{total}} = \mathbf{S}_{\text{smoothing}} + \mathbf{S}_{\text{meas}} + \mathbf{S}_{\text{mod.param.}} \quad (10)$$

2.3 Data analysis

For the retrievals, we use the same ILS as in previous studies by (Barret et al., 2005 and Coheur et al., 2005). The *a priori* state vector $\mathbf{x}_a$, the *a priori* covariance matrix $\mathbf{S}_a$, and additional input parameters, including the pressure and the temperature profiles, have been built based on data from the European Center for Medium Range Weather Forecasts (ECMWF). The *a priori* information used for the IMG period analyzed here, comes from a latitudinal set (+90°,+60°), (+60°,+23°), (+23°,–23°), (–23°,–60°) and (–60°,–90°) of profiles averaged over 3 years (1995, 1996, 1997). It covers altitudes ranging from the ground to 44 km by step of 2 km. The spectroscopic parameters were extracted from the HITRAN 2004 database (Rothman et al., 2005). The noise equivalent spectral radiance σ_ε of the IMG instrument was estimated to be of the order of 2×10^{-9} W/(cm^2 cm^{-1} sr) (Kobayashi et al., 1999). However, the level of noise varies strongly with spectral bands and latitudes. In order to constrain the retrievals, a value of σ_ε close to the best Root Mean Squares (RMS) has been set (Fig. 1).

Water vapour absorbs all over the spectral domain of IMG, but many strong absorption lines (Clerbaux et al., 2003) overlap and/or saturate the absorption. On this basis, we have selected one micro-window within band 3 for the retrieval of HOD, extending from 1 205.40 to 1 227.50 cm^{-1}, and two windows within band 2 for the retrieval of $H_2^{18}O$, extending respectively from 2004.00 to 2015.32 and 2019.6 to 2032.00 cm^{-1}. Figure 1 gives a typical example of spectral fit in the selected windows. The fit is good in both bands, with the residual spectra (Observed-Calculated) being close to the expected instrumental noise value.

The VMR for the different water isotopologues are retrieved on 10 vertical levels, in the middle of layers extending from the ground to 20 km as follow : 0–1, 1–3, 3–5, 5–7, 7–9, 9–11, 11–13, 13–15, 15–17 and 17–20 km. In the spectral range used, CH_4, $H_2^{17}O$ and CO_2 profiles are fixed to standard values. The surface Temperature (Ts) and the profiles of $H_2^{16}O$, HOD and $H_2^{18}O$ are adjusted simultaneously.

3 Comparison with sondes

3.1 Retrievals and characterizations

This section aims to give insight onto the capabilities of the IMG measurements for determining the vertical profiles of $H_2^{16}O$, HOD and $H_2^{18}O$ in the troposphere, rather than to perform a quantitative validation of the results. However, in order to ensure that the large scale features of the water distribution on the horizontal and vertical dimensions are well reproduced, we have chosen to compare the retrieved profiles to a restricted set of correlative humidity soundings representative of different latitudes. The latter have been selected from regular balloon launches performed by the Network for the Detection of Atmospheric Composition Change (NDACC) and the World Ozone and Ultraviolet Data Center (WOUDC) in the time period of interest. A set of spectra within 3° latitude/longitude of the eight NDSC or WOUDC stations and measured within one day of the soundings has been considered (Table 1). Since the sonde measurements are performed at a very high vertical resolution, they need to be smoothed in order to account for the lower resolution of the IMG observing system and thus to allow a meaningful comparison with the retrieved profiles. The smoothed water vapour sonde profiles $\mathbf{x}_s$ are calculated from the measured profiles $\mathbf{x}_{\text{sonde}}$ according to (Rodgers, 2000):

$$\mathbf{x}_s = \mathbf{x}_a + \mathbf{A}(\mathbf{x}_{\text{sonde}} - \mathbf{x}_a) \quad (11)$$

ACPD
7, 4857–4888, 2007

EGU

Figure 2 shows the comparisons for each coincident IMG/sonde measurement. In all cases, the retrieved profiles are in good agreement with the sonde measurements over the entire altitude range covered (0–16 km). Although not shown in Fig. 2, it is interesting to point out that the retrieved $H_2^{16}O$ profiles from band 2 are very similar to those retrieved from Band 3, the discrepancies for each layer being less than their respective uncertainty.

In light of Fig. 2, we can safely conclude that the retrievals provide a good representation of the general shape of the water vapour profile in the troposphere. In particular, they reproduce adequately the large latitudinal variations but also the altitude gradients up to the tropopause. For tropical values (Hilo, Samoa and Suva), the volume mixing ratio is almost one order of magnitude greater than in the highest latitudes and the variation with altitude is important, since more than 90% of the water vapour amount is found between the ground and 6 km. Furthermore, the comparison between the retrieved profiles and the local sonde measurements does not reveal any systematic discrepancy or any dependency with the water vapour amount. The disagreement between the satellite derived values and the sonde data is largest above 4 km, probably as a result of the coincidence criterion, which is loose considering the fast spatial and temporal variation of the water vapour amount (see Table 1). In spite of this, the comparisons highlight the ability of the thermal infrared nadir measurements to provide vertically resolved profiles of water vapour over the entire altitude range of the troposphere, possibly up to the UT/LS region.

The high sensitivity of the IMG measurements to the $H_2^{16}O$ vertical distribution, and to a lower extent to that of the heavier isotopologues, is further illustrated in Fig. 3, for a case corresponding to a high DOFS. Figure 3a shows the retrieved profiles, starting from an *a priori* profile for the heavier isotopologues ($H_2^{18}O$, HOD) which is the same as the principal one ($H_2^{16}O$), but divided by their respective SMOW ratio. It is seen that the retrieved profiles exhibit similar structures despite the fact that they are retrieved without correlations. These profiles do not allow, as such, the detection of any unexpected evolution in the isotopologic vertical distribution.

The averaging kernels associated with these retrievals are shown on Fig. 3b. The measurements contain information up to 12 km in altitude for $H_2^{16}O$ and 10 km for HOD and $H_2^{18}O$. For the case shown here, the amount of information is characterized by a DOFS of 5.0 for $H_2^{16}O$, 2.6 for HOD and 2.3 for $H_2^{18}O$. The information on the isotopologic ratios, which will be discussed next, is obviously limited by the lowest information content, here HOD and $H_2^{18}O$.

Error budget as a function of altitude is displayed in Fig. 3c. The different curves correspond to the square root of the diagonal elements of the error covariance matrices calculated according to Eqs. (7) to (10). The error analysis confirms that the retrievals are mainly driven by *a priori* information above 16 km for all isotopologic species. For $H_2^{16}O$, the principal contributing errors are the smoothing and the measurement errors. For the heavier isotopologues the smoothing error is dominant. Additional contributions to the total retrieval error, including the simultaneous retrievals of the surface temperature and interfering species, are found to be very weak (less than 1%). The total error is particularly small near the surface, where the sensitivity is maximum, with errors reaching 6% for $H_2^{16}O$, 14% and 12% for HOD and $H_2^{18}O$ respectively. The total errors are smaller than 20% for $H_2^{16}O$, and than 30% for the heavier isotopologues throughout the troposphere, which is a substantial improvement with respect to the *a priori* variability. The most significant improvement is located in the troposphere around 6 km, where the *a priori* uncertainty is 90 %.

The present analysis of the information content shows similarities with the results previously obtained from IMG by Zakharov et al. (2004) for tropospheric $H_2^{16}O$. On the contrary, we find a higher sensitivity for HOD, than in their earlier work, which reports on a single piece of information located in 3–5 km height. This is very likely due to the larger spectral interval considered in the present study as compared to that use in the Zakharov et al. (2004) paper.

ACPD
7, 4857–4888, 2007

3.2 Isotopologic composition of water vapour

Depletion of heavier water isotopologues relative to the SMOW standard is measured in parts per mil using the conventional δ notation. It is defined as:

$$\delta = \left(\frac{R}{R_{SMOW}} - 1 \right) \times 1000 \quad (12)$$

Where R denotes the isotopologic mass ratio, i.e. $H_2^{18}O/H_2^{16}O = 2.0052.10^{-3}$ and $HDO/H_2^{16}O = 0.31152.10^{-3}$.

The major source of atmospheric water vapour is the ocean. It is characterized by a SMOW isotopologic composition (δ =0‰). As explained in the introduction, isotopologically heavier molecules have lower vapour pressure than the main isotopologue, leading to isotopologic fractionation between the phases during condensation and evaporation processes. The fractionation associated with the equilibrium exchange reaction can be expressed using the isotopologue fractionation factor α:

$$\alpha = R_C / R_V \quad (13)$$

where R_C and R_V are the isotopologue ratios of the condensed and vapour phases, respectively. The sign and magnitude of α depend on many factors, the most important of which is temperature. This fractionation leads to the typical values of $\delta^{18}O$=–12‰ and δD=–85‰ just above the ocean (Bechtel et al., 2003). When saturated air is lofted and cooled, the heavier isotopologues, which condense more readily, are removed and the isotopologic ratios decrease with altitude. As a consequence, R_V of the remaining vapour decreases monotonically. In the thermodynamic equilibrium approximation, R_V is described by the Rayleigh equation:

$$R_V = R_0 f^{(\alpha-1)} \quad (14)$$

Where R_0 is the initial isotopologic ratio in the liquid water, f is the remaining vapour fraction and α is the equilibrium fractionation factor during evaporation.

The composition of water isotopologues is affected by complex meteorological processes that provide a characteristic fingerprint of their origin.

In addition to the phase changes under equilibrium conditions, the kinetic effect resulting from a different diffusivity for each isotopologue can be taken into account. The higher diffusivity of HOD, compared to $H_2^{18}O$, results in an additional separation. Humidity relative to saturation at sea surface temperature and wind speed are the major controlling factors. As a consequence, depletion of isotopologic water ratios is associated with cold regions and enhancements are found in warm regions. This partitioning is now recognized as a tool for characterizing groundwater from different environments, and is described by the Meteoric Water Line (Bowen et al., 2003; Coffey et al., 2006; Bechtel et al., 2003):

$$\delta D = 8\delta^{18}\mathrm{O} + 10‰\,(\mathrm{SMOW}) \quad (15)$$

The concept of the deuterium excess is then defined from Eq. (15) as: $d=\delta D - 8\delta^{18}O$. Climatic information about the conditions of temperature and humidity prevailing at the evaporative source of the vapour can be inferred from the study of d.

In light of the averaging kernels and error budgets of Fig. 3, we have restricted the study of the isotopologues depletion to altitudes ranging between 0 and 8 km (see Fig. 4 for the retrieval at Suva). The δD, $\delta^{18}O$ and d-excess calculated from Eq. (12) are obtained using the $H_2^{16}O$, HOD and $H_2^{18}O$ VMR values retrieved independently (i.e. without correlations between the isotopologic species). The δD and $\delta^{18}O$ vertical distributions in Fig. 4 exhibit the expected general decay with altitude. The δ values and their uncertainties are consistent with those reported in the literature, with different experimental techniques (Gettelman et al., 2005; Ehhalt et al., 2005) and δD profile, in particular, can be compared with the results obtained from TES by (Worden et al., 2006) between 850 and 300 hPa with a sensitivity peak at around 700 hPa.

Few previous studies have reported d-excess values (Armengaud et al., 1998; Masson-delmotte et al., 2005; Bowen et al., 2003), essentially because it is calculated from very weak variations of the values, so that it needs high sensitivity instruments.

ACPD
7, 4857–4888, 2007

For the example of Fig. 4, the uncertainty on the calculation of the *d*-excess are very important and even encompass the mean value (i.e. 10%), which points towards the limitations of the retrievals for the analyses of this quantity. Nevertheless, it is worth pointing out that the negative value at 2 km is correlated with an important increase of the Relative Humidity (see Table 2), which is perfectly consistent with the pattern suggested by Bowen et al. (2003). It would be interesting to use the *d*-excess values on the global scale to improve our understanding of the regional diversity, but since HOD and $H_2^{18}O$ are retrieved from adjacent scenes on the ground, this can not be undertaken here.

4 Global distributions

For global distribution mapping, only cloud free spectra were selected, using adequate filtering in bands 2 and 3 (Hadji-Lazaro, et al., 2001; Wespes, et al., 2007). Moreover, a filtering based on the spectral root mean square value after retrieval allows discarding excessively noisy spectra. All the global distributions presented here are averaged on a 5° latitude by 10° longitude grid.

Figure 5 shows the global distributions of the DOFS for $H_2^{16}O$, $H_2^{18}O$ and HOD. As discussed in previous studies (Barret, et al., 2005; Coheur, et al., 2005), a latitudinal dependency of the DOFS, which follows the temperature variations, is observed. As a consequence, high DOFS are found in the tropics, where high surface temperature leads to a higher signal. On the opposite, high latitude regions have lower surface temperature and low DOFS. The effect is mostly pronounced for the heavier isotopologues, whose evaporation are more strongly correlated to temperature. For this reason, the measurements polewards of 60° latitude have been rejected. In-between these limits, the DOFS ranges from 1 to 5 with a mean value of 3 (see Fig. 5) for $H_2^{16}O$. The difference between the DOFS distribution pattern of HOD and $H_2^{18}O$ is linked to the better signal-to-noise ratio achieved in band 3 where HOD is retrieved.

In order to avoid discussing results which depend upon the vertical sensitivity of the

measurements to the different isotopologues, we focus hereafter on the global distributions of tropospheric $H_2^{16}O$, $H_2^{18}O$ and HOD, expressed as a column integrated between 0 and 16 km. They are presented in Fig. 6, along with the latitudinal averaged distributions of the profiles. The measured partial columns range are from about 0.04 to 0.4×10^{24}, 0.08 to 0.8×10^{21} and 0.1 to 1.2×10^{20} molecules.cm^{-2} for $H_2^{16}O$, $H_2^{18}O$ and HOD, respectively. Higher abundances are found within the inter-tropical belt. This latitudinal effect is also clearly seen on the latitudinal distributions, with strong impact of surface temperatures and tropopause altitudes on the retrieved profiles. Globally, the water amounts are larger in southern hemisphere, but some local exceptions are visible. For instance, at 40° N, a peak of concentration is observed for $H_2^{16}O$ and $H_2^{18}O$. Despite the limited vertical sensitivity of the measurements, large latitudinal and regional variability are also observed, which are most probably linked to a mixing of various air masses (in equatorial regions for example).

On the zonal distribution maps, we observe a clear Ocean-Continent contrast for all isotopologues, in particular above Europe, North America, Australia and for high altitude regions. The latter effect is explained by atmospheric dehydration with precipitation. At the opposite, the very moist equatorial forests are observed, like in Amazonia, central Africa and Indonesia. These observations are consistent with water vapour global distribution from TES, obtained by Worden et al. (2007)

The distributions of the isotopologic ratios, given in Fig. 7, show a wide range of isotopologic depletion values: δD is indeed between 0 and –800 ‰, while $\delta^{18}O$ ranges between 0 and –150‰. The latitudinal distribution also reveals a very large variability of both δ values with altitude in the troposphere, consistent with the observation of Webster et al. (2003). The less depleted values of $\delta^{18}O$ and δD are principally found into the tropics (+20°;–20°). At these latitudes, the maximum values of δD are located between the ground and 2 km and they are quasi-constant above 10 km (see Fig. 7a) as suggested by previous work (Kuang et al., 2003). For $\delta^{18}O$, there is an important contrast between the 6–14 km region, where $H_2^{18}O$ is the most depleted and the higher altitudes, where the $\delta^{18}O$ values raise up (see Fig. 7b). This could be explained by the

ACPD
7, 4857–4888, 2007

EGU

fact that the vapour from equatorial forest evapotranspiration (Amazonia and Africa) is not lofted above 6 km and therefore cannot participate to isotopic enrichment (Gat et al., 1991). The increase of δ values near the tropopause observed for the two species is likely due to a combination of descending water vapour from the stratosphere, which is enriched in heavier isotopologic species, for instance by interaction with reservoir molecules (Zahn et al., 2006) or ice lofting process (Franz et al., 2005; Gettelman et al., 2005; Keith, 2000; Ehhalt et al., 2005). This effect globally increases from the equator towards the poles. Finally, local isotopologic enrichment is probably the result of complex convective activity (Kuang et al., 2003; Hanisco et al., 2006).

The zonal mean distributions highlight regions where $\delta^{18}O$ and δD decrease. This is the case, for instance, for regions characterized by important depletion, like Northern America and Eastern Europe, which are correlated with low temperatures and Ocean-Continent effect due to the progressive depletion during rainout (see Fig. 7a). The fact that the latter is lower for the Amazonian Basin and Equatorial Africa could be explained by an important contribution of the re-evaporated moisture in convective regions (Lawrence et al., 2004) smoothed by the partial columns representation. On the contrary, regional increases of δD and $\delta^{18}O$ are observed, as in Eastern Africa or Northern Australia. This can be explained by the lofting of less depleted water vapour, which is characteristic of arid regions. The other local events observed on these distributions are difficult to analyze in details due to the large uncertainty on the measurements. Globally, the results presented here show the potential of high-resolution nadir spectra to study isotopologic evolution of troposheric water vapour and hence provide information about the water cycle on a large scale.

5 Conclusions

A set of high–resolution Fourier transform nadir spectra measured by the IMG instrument between 1 and 10 April 1997 has been used to obtain quasi-global distributions of three isotopologic species of water vapour (i.e. $H_2^{16}O$, $H_2^{18}O$ and HOD) in the tropo-

sphere. For $H_2^{18}O$ these are the first reported global distributions. The retrievals were made using a software relying on the OEM allowing to measure volume mixing ratios and partial columns from the ground up to 16 km.

The comparison of the retrievals profiles with coincident sonde measurements, performed at a series of representative latitudes, has revealed the potential of the satellite measurements to capture the spatial variations of the water vapour amount in the troposphere. The characterization of the profiles showed that the measurements contain up to 5, 3 and 2.3 independent pieces of information on the $H_2^{16}O$, HOD and $H_2^{18}O$ vertical distributions, respectively. On the basis of the errors and averaging kernels analyses, it was found that the sensitivity was maximal between the ground and 12 km for $H_2^{16}O$ and between the ground and 8 km for the others isotopologic species. The uncertainties on the tropospheric profiles are less than 20% for the principal isotopologue and 30% for the others, improving significantly the prior knowledge. On a case study, we were able to show that the calculated δD and $\delta^{18}O$ vertical distributions exhibit decay with altitude. Moreover, although the isotopologic ratios determinations are not accurate enough to calculate significant values of the d-excess, the vertical structure seems to be correlated with the Relative Humidity amount, as expected.

The $H_2^{16}O$, $H_2^{18}O$ and HOD zonal and latitudinal distributions of partial columns in the troposphere have been presented. They showed the variation of the tropopause height and the surface temperature effect on the water vapour amount, the latter being more important for heavier isotopologues. Some Ocean-Continent differences and altitude effects were also observed and discussed. The global distributions of isotopologic ratios allowed observing that the depletion of heavier water vapour isotopologues is more important at higher altitudes and higher latitudes. Some regional variations have been highlighted, but the uncertainties on the retrieved quantities and the low vertical sensitivity have limited the geophysical analysis of the results.

Globally, the results have demonstrated the ability of infrared spectroscopy from space to study many tropospheric processes for which water vapour and isotopologues play a significant role from the local to the global scale. The results open promising per-

ACPD
7, 4857–4888, 2007

spectives for future space missions. This will be the case for the Infrared Atmospheric Sounding Interferometer (IASI) onboard MetOp platforms (Clerbaux et al., 2007) whose data are expected to improve our understanding of the chemistry, transport and climate.

Acknowledgements. The research was funded by the Fonds National de la Recherche Scientifique (FNRS, Belgium), the Belgian State Federal Office for Scientific, Technical and Cultural Affairs and the European Space Agency (ESA-Prodex arrangement C90-220). Financial support by the "Actions de Recherche Concertées" (Communauté Française de Belgique) is also acknowledged. This work was undertaken in the framework of the ISSWG (IASI Sounding Science Working Group) activities under the auspices of EUMETSAT (European Organization for the Exploitation of Meteorological Satellites) and CNES (Centre National d'Etudes Spatiales). The authors are grateful to IMGDIS/ERSDAC for providing the IMG level 1 data. ECMWF ERA-40 data used in this study have been obtained from the ECMWF data server. Several data used in this publication were obtained as part of the Network for the Detection of Atmospheric Composition Change (NDACC) and the World Ozone and Ultraviolet Radiation Data Centre (WOUDC) and are publicly available (see http://www.ndsc.ncep.noaa.gov, http://www.woudc.org/).

References

Armengaud, A., Koster, R. D., Jouzel, J., and Ciais, P.: Deuterium excess in Greenland snow: Analysis with simple and complex models, J. Geophys. Res., 103, D8, 8947, doi:10.1029/98JD00274, 1998.

Barret, B., Turquety, S., Hurtmans, D., Clerbaux, C., Hadji-Lazaro, J., Bey, I., Auvray, M., and Coheur, P.-F.: Global carbon monoxide vertical distributions from spaceborne high-resolution FTIR nadir measurements, Atmos. Chem. Phys., 5, 2901–2914, 2005, http://www.atmos-chem-phys.net/5/2901/2005/.

Bechtel, C. and Zahn, A.: The isotopologue composition of water vapour: A powerful tool to study transport and chemistry of middle atmospheric water vapour, Atmos. Chem. Phys. Discuss., 3, 3991–4036, 2003, http://www.atmos-chem-phys-discuss.net/3/3991/2003/.

Bowen, G. J. and Revenaugh, J.: Interpolating the isotopologic composition of modern meteoric precipitation, Water Resour. Res., 39(10), 1299, doi:10.1029/2003WR002086, 2003.

Ciais, P. and Jouzel, J.: Deuterium and oxygen 18 in precipitation: Isotopologic model, including mixed cloud processes, J. Geophys. Res., 99, D8, 16793, doi:10.1029/94JD00412, 1994.
Clerbaux, C., Hadji-Lazaro, J., Turquety, S., Mégie, G., and Coheur, P.-F.: Trace gas measurements from infrared satellite for chemistry and climate applications, Atmos. Chem. Phys., 3, 1495–1508, 2003, http://www.atmos-chem-phys.net/3/1495/2003/.
Clerbaux, C., Hadji-Lazaro, J., Turquety, S., George, M., Coheur, P.-F., Hurtmans, D., Wespes, C., Herbin, H., Blumstein, D., Tournier, B., and Phulpin, T.: The IASI/MetOp mission: first observations and highlight of its potential contribution to the GMES Earth observation component, Space Res. Today, in press, 2007.
Clough, S. A., Shephard, M. W., Mlawer, E., Delamere, J. S., Iacono M., Cady-Pereira, K., Boukabara, S., and Brown, P. D.: Atmospheric radiative transfer modeling: A summary of the AER codes, J. Quant. Spectrosc. Radiat. Transf., 91, 233–244, 2005.
Coffey, M. T., Hannigan, J. W., and Goldman, A.: Observations of upper tropospheric/lower stratospheric water vapour and its isotopologues, J. Geophys. Res., 111, D14, doi:10.1029/2005JD006093, 2006.
Coheur, P.-F., Barret, B., Turquety, S., Hurtmans, D., Hadji-Lazaro, J., and Clerbaux, C.: Retrieval and characterization of ozone vertical profiles from a thermal infrared nadir sounder, J. Geophys. Res., 110, D24, doi:10.1029/2005JD005845, 2005.
Ehhalt, D. H., Rohrer, F., and Fried, A.: Vertical profiles of HDO/H_2O in the troposphere, J. Geophys. Res., 110, D13, doi:10.1029/2004JD005569, 2005.
Forster, P. M. D. and Shine, K. P.: Assessing the climate impact of trends in stratospheric water vapour, Geophys. Res. Lett., 29 (6), 1086, doi:10.1029/2001GL013909, 2002.
Franz, P. and Rockmann, T.: High-precision isotopologue measurements of $H_2{}^{16}O$, $H_2{}^{17}O$, $H_2{}^{18}O$, and the $\Delta^{17}O$-anomaly of water vapour in the southern lowermost stratosphere, Atmos. Chem. Phys., 5, 2949–2959, 2005, http://www.atmos-chem-phys.net/5/2949/2005/.
Gat, J. R. and Matsui, E.: Atmospheric water balance in the Amazon basin: an isotopic evapotranspiration model, J. Geophys. Res., 96, 13 179–13 188, 1991.
Gedzelman, S., Hindman, E., Zhang, X., Lawrence, J., Gamache, J., Black, M., Black, R., Dunion, J., and Willoughby, H.: Probing Hurricanes with stable isotopologues of rain and water vapour, Mon. Weather Rev., 131, 1112–1127, 2003.
Gettelman, A. and Webster, C. R.: Simulations of water isotopologue abundances in the upper troposphere and lower stratosphere and implications for stratosphere troposphere exchange, J. Geophys. Res., 110, D17, doi:10.1029/2004JD004812, 2005.

Hadji-Lazaro, J., Clerbaux, C., Couvert, P., Chazette, P., and Boone, C.: Cloud filter for CO retrieval from IMG infrared spectra using ECMWF temperatures and POLDER cloud data, Geophys. Res. Lett., 28(12), 2397, doi:10.1029/2000GL012342, 2001.

Hanisco, T. F., Moyer, E. J., Weinstock, E. M., St. Clair, J. M., Sayres, D. S., Smith, J. B., Lockwood, R., and Anderson J. G.: Observations of deep convective influence on stratospheric water vapor and its isotopic composition, Geophys. Res. Lett., 34, L04814, doi:10.1029/2006GL027899, 2007.

Hartmann, D. L.: Climate Change : Tropical Surprises, Science, 295, 811–812, 2002.

Jouzel, J., Alley, R. B., Cuffey, K. M., Dansgaard, W., Grootes, P., Hoffmann, G., Johnsen, S. J., Koster, R. D., Peel, D., Shuman, C. A., Stievenard, M., Stuiver, M., and White, J.: Validity of the temperature reconstruction from water isotopologues in ice cores, J. Geophys. Res., 102, C12, 26471, doi:10.1029/97JC01283, 1997.

Keith, D. W.: Stratosphere-troposphere exchange: Inferences from the isotopic composition of water vapor, J. Geophys. Res., 105, D12, 15167, doi:10.1029/2000JD900130, 2000.

Kirk-Davidoff, D. B., Hintsa, E. J., Anderson, J. G., and Keith, D. W.: The effect of climate change on ozone depletion through changes in stratospheric water vapour, Nature, 402, 399–401, 1999.

Kobayashi, H., Shimota, A., Kondo, K., Okumura, E., Kameda, Y., Shimoda, H., and Ogawa, T.: Development and evaluation of the interferometric monitor for greenhouse gases: A high-throughput Fourier-transform infrared radiometer for nadir Earth observation, Appl. Optics, 38, 6801–6807, 1999.

Kuang, Z. M., Toon, G. C., Wennberg, P. O., and Yung, Y. L.: Measured HDO/H2O ratios across the tropical tropopause, Geophys. Res. Lett., 30(7), 1372, doi:10.1029/2003GL017023, 2003.

Lawrence, J. R., Gedzelman, S. D., Gamache, J., and Black, M.: Stable isotopologue ratios: Hurricane Olivia, J. Atmos. Chem., 41, 67–82, 2002.

Lawrence, J. R., Gedzelman, S. D., Dexheimer, D., Cho, H.-K., Carrie, G. D., Gasparini, R., Anderson, C. R., Bowman, K. P., and Biggerstaff, M. I.: Stable isotopic composition of water vapor in the tropics, 109, D06, doi:10.1029/2003JD004046, 2004.

Masson-Delmotte, V., Jouzel, J., Landais, A., Stievenard, M., Johnsen, S. J., White, J. W. C., Werner, M., Sveinbjornsdottir, A., and Fuhrer, K.: GRIP Deuterium excess reveals rapid and orbital-scale changes in Greenland moisture origin, Science, 309, 118–121, 2005.

McCarthy, M. C., Boering, K. A., Rahn, T., Eiler, J. M., Rice, A. L., Tyler, S. C., Schauffler,

S., Atlas, E., and Johnson, D. G.: The hydrogen isotopologic composition of water vapour entering the stratosphere inferred from high-precision measurements of D-CH^4 and D-H_2, J. Geophys. Res., 109, D07, doi:10.1029/2003JD004003, 2004.
Moyer, E. J., Irion, R. W., Yung, Y. L., and Gunson, M. R.: ATMOS stratospheric deuterated water vapour and implications for troposphere-stratosphere transport, Geophys. Res. Lett., 23(17), 2385, doi:10.1029/96GL01489, 1996.
Rodgers, C. D.: Inverse Methods for Atmospheric Sounding: Theory and Practice, World Sci., Hackensack, N. J, 2000.
Rosenlof, K. H., Oltmans, S. J., Kley, D., Russell, J. M., Chiou, E.-W., Chu, W. P., Johnson, D. G., Kelly, K. K., Michelsen, H. A., Nedoluha, G. E., Remsberg, E. E., Toon, G. C., McCormick, M. P.: Stratospheric water vapour increases over the past half-century, Geophys. Res. Lett., 28(7), 1195, doi:10.1029/2000GL012502, 2001.
Rosenlof, K. H.: How water enters the stratosphere, Science, 302, 1691–1692, 2003.
Rothman, L. S., Jacquemart, D., Barbe, A., Chris Benner, D., Birk, M., Brown, L. R., Carleer, M. R., Chackerian Jr., C., Chance, K., Coudert, L. H., Dana, V., Devi, V. M., Flaud, J.-M., Gamache, R. R., Goldman, A., Hartmann, J.-M., Jucks, K. W., Maki, A. G., Mandin, J.-Y., Massie, S. T., Orphal, J., Perrin, A., Rinsland, C. P., Smith, M. A. H., Tennyson, J., Tolchenov, R. N., Toth, R. A., Vander Auwera, J., Varanasi, P., Wagner G.: The HITRAN 2004 molecular spectroscopic database, J. Quant. Spectrosc. Radiat. Transf., 96, 139–204, 2005.
Schmidt, G. A., Hoffmann, G., Shindell, D. T., and Hu, Y.: Modelling atmospheric stable water isotopologues and the potential for constraining cloud processes and stratosphere-troposphere water exchange, J. Geophys. Res., 110, D21, doi:10.1029/2005JD005790, 2005.
Schneider, E. K., Kirtman, B. P., and Lindzen, R. S.: Tropospheric Water Vapour and Climate Sensitivity, J. Atmos. Sci., 56, 1649–1658, 1999.
Shindell, D. T.: Climate and ozone response to increased stratospheric water vapour, Geophys. Res. Lett., 28(8), 1551, doi:10.1029/1999GL011197, 2001.
Smith, R.B.: Deuterium in North Atlantic storm tops, J. Atmos. Sci., 49, 2041–2057, 1992.
Solomon, S.: Stratospheric ozone depletion: A review of concepts and history, Rev. Geophys., 37, 275–316, 1999.
Strong, M., Scharp, Z. D., and Gutzler, D. S.: Diagnosing moisture transport using D/H ratios of water vapor, Geophys. Res. Lett., 34, L03404, doi:10.1029/2006GL028307, 2007.
Tabazadeh, A., Santee, M. L., Danilin, M. Y., Pumphrey, H. C., Newman, P. A., Hamill, P. J.,

and Mergenthaler, J. L.: Quantifying denitrification and its effect on ozone recovery, Science, 288, 1407–1411, 2000.

Webster, C. R. and Heymsfield, A. J.: Water isotopologue ratios D/H, $^{18}O/^{16}O$, $^{17}O/^{16}O$ in and out of clouds map dehydration pathways, Science, 302, 1742–1745, 2003.

Wespes, C., Hurtmans, D., Herbin, H., Barret, B., Turquety, S., Hadji Lazaro, J., Clerbaux, C. and Coheur, P.-F.: Satellite measurements of nitric acid global distributions in the troposphere and the stratosphere, J. Geophys. Res., in press, 2007.

Worden, J., Bowman, K., Noone, D., Beer, R., Clough, S., Eldering, A., Fisher, B., Goldman, A., Gunson, M., Herman, R., Kulawik, S. S., Lampel, M., Luo, M., Osterman, G., Rinsland, C., Rodgers, C., Sander, S., Shephard, M., and Worden, H.: Tropospheric Emission Spectrometer observations of the tropospheric HDO/H2O ratio: Estimation approach and characterization, J. Geophys. Res., 111, D16, doi:10.1029/2005JD006606, 2006.

Worden, J., Noone, D., Bowman, K., Beer, R., Clough, S., Eldering, A., Fisher, B., Gunson, M., Goldman, A., Herman, R., Kulawik, S. S., Lampel, M., Osterman, G., Rinsland, C., Rodgers, C., Sander, S., Shephard, M., Webster, C. R. and Worden, H.: Importance of rain evaporation and terrestrial sources in the tropical water cycle, Nature, 445, 528–532, 2007.

Zahn, A., Franz, P., Bechtel, C., Groo, J.-U., and Rckmann, T.: Modelling the budget of middle atmospheric water vapour isotopologues, Atmos. Chem. Phys., 6, 2073–2090, 2006, http://www.atmos-chem-phys.net/6/2073/2006/.

Zakharov, V. I., Imasu, R., Gribanov, K. G., Hoffmann, G., and Jouzel, J.: Latitudinal distribution of the deuterium to hydrogen ratio in the atmospheric water vapour retrieved from IMG/ADEOS data, Geophys. Res. Lett., 31, L12104, doi:10.1029/2004GL019433, 2004.

Table 1. Summary of the coincident IMG and water vapour sonde measurements.

Observing Site	Sonde: Latitude, Longitude, Altitude	Day (April 1997) and Time of Sonde measurement (UTC)	IMG: Latitude, Longitude	Day (April 1997) and Time of IMG measurement (UTC)
Ny-Aalesund	78.93°, 11.95°, 11 m	10, 5 h 49 m	79.62°, 11.87°	10, 13 h 39 m
Uccle	50.80°, 4.35°, 100 m	07, 10 h 18 m	51.12°, 6.23°	07, 21 h 32 m
Wallops	37.84°, –75.48°, 13 m	09, 14 h 57 m	35.74°, –73.83°	09, 16 h 01 m
Hilo	19.72°, –155.08°, 11 m	09, 18h38m	21.83°, –154.12°	09, 8h 44 m
Samoa	–14.23°, –170.56°, 82 m	04, 13 h 42 m	–10.27°, –169.11°	04, 21 h 51 m
Suva	–18.10°, 178.20°, 6 m	04, 22h00m	–18.37°, 174.64°	04, 11 h 15 m
Lauder	–45.04°, 169.68°, 370 m	02, 01h58m	–44.86°, 168.13°	02, 22 h 55 m
Neumayer	–70.65°, –8.26°, 42 m	05, 15 h 18 m	–67.59°, –9.13°	05, 09 h 55 m

ACPD
7, 4857–4888, 2007

Table 2. Retrieval parameters from the Suva IMG spectrum.

Altitude (km)	Pressure (hPa)	Temperature (K)	Relative Humidity (%)
0	1000	295.5	66.61
2	809	284.0	96.61
4	635	279.2	67.08
6	495	265.7	91.42
8	380	250.5	34.10

ACPD
7, 4857–4888, 2007

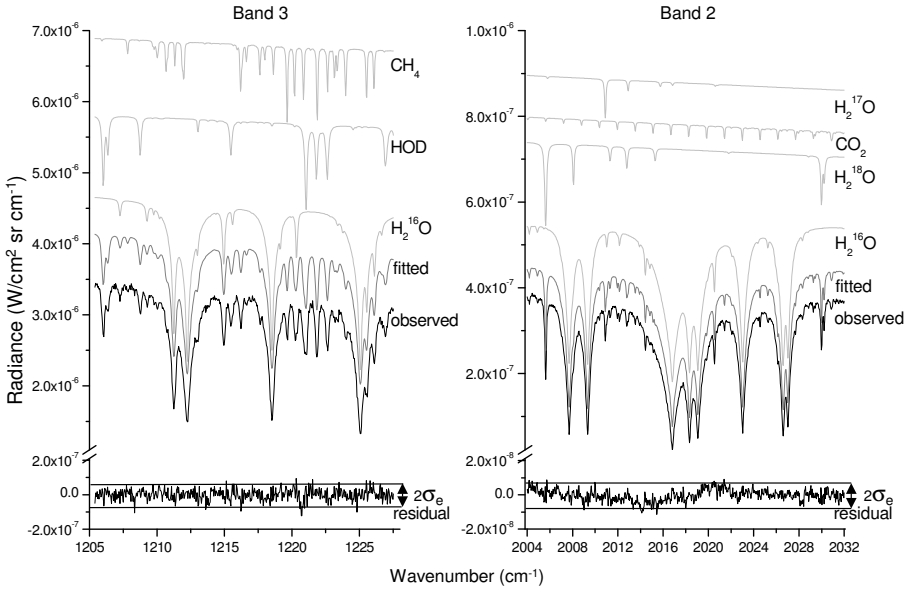

Fig. 1. Spectral micro-windows used for retrieving $H_2^{16}O$, $H_2^{18}O$ and HOD profiles. Top and middle: IMG radiance spectra and principal individual contributions of the main absorbers in the IMG band 2 and band 3 spectral ranges. Bottom: Residuals (observed-calculated spectra), plotted with an expanded scale and compared to the σ_ε value.

ACPD
7, 4857–4888, 2007

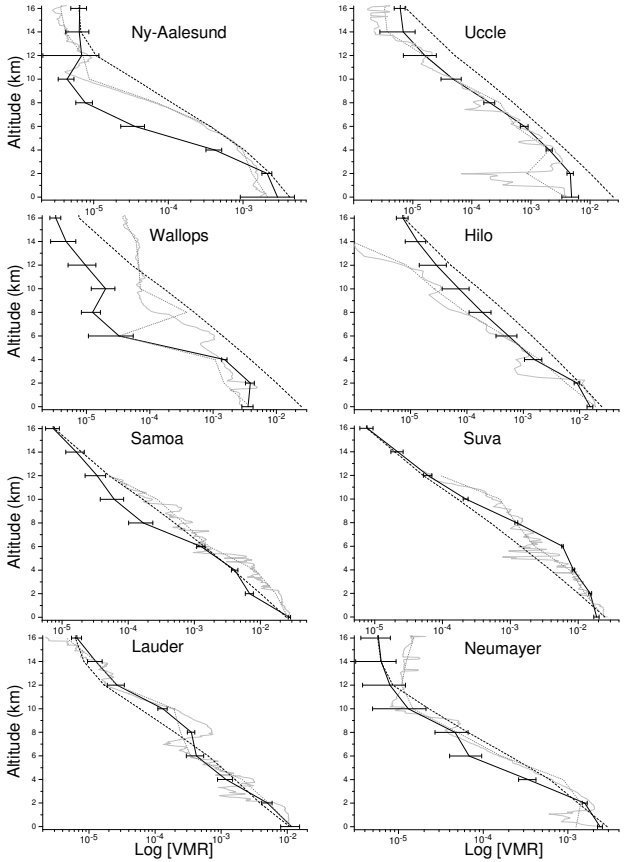

Fig. 2. Retrieved water vapour profiles (VMR) up to 16 km from IMG observations between 1 and 10 April 1997 for eight different sites compared with water vapour sonde measurements (see Table 1). The retrieved values are indicated by black lines, the *a priori* profiles by black dashes, the sonde profiles by grey lines and the smoothed sonde profiles by grey dots.

ACPD
7, 4857–4888, 2007

EGU

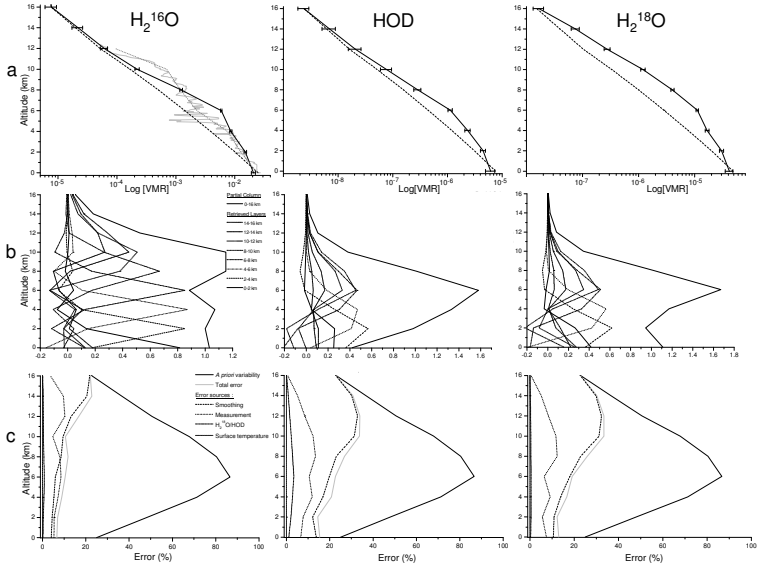

Fig. 3. Example of results obtained for a typical scene corresponding to tropical latitudes. **(a)** Retrieved $H_2^{16}O$, $H_2^{18}O$ and HOD profiles in VMR units and comparison with a water vapour sonde measurement at Suva. The grey and black lines represent the sonde and retrieved profiles respectively. The grey dots are the smoothed sonde and the black dashes are the *a priori* profiles. The *a priori* profiles for $H_2^{18}O$ and HOD were taken to be the same as $H_2^{16}O$ multiplied by the standard isotopologic ratios. **(b)** Averaging kernels, in volume mixing ratio units, for the three isotopologues. The averaging kernels for the eight retrieved layers are shown, as well as those for the 0–16 km (black lines) columns, representative of the vertical information contained in the measurements. Degrees of freedom for signal are respectively 5, 2.6 and 2.3 for $H_2^{16}O$, HOD and $H_2^{18}O$. **(c)** Error profiles. The curves are the square root of the diagonal elements of the prior and posterior error covariance matrices (Eq. 7 to 10). For computing the errors due to the temperature profiles, uncorrelated uncertainty of 1 K is assumed. The errors due to the uncertainties on the others species (i.e. $H_2^{17}O$, CH_4, CO_2) are negligible and therefore not shown.

ACPD
7, 4857–4888, 2007

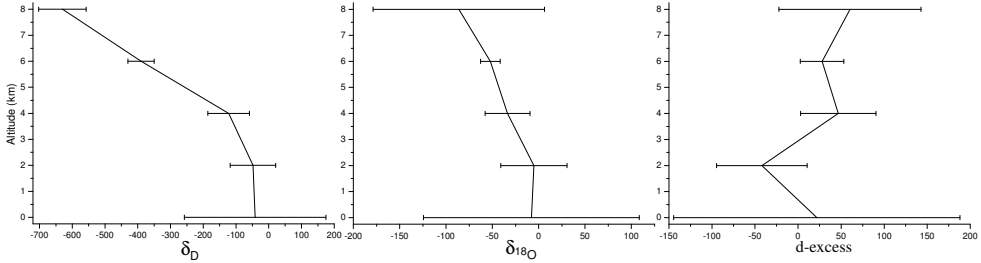

Fig. 4. Example of δD, $\delta^{18}O$ isotopologic ratios and d-excess vertical profiles between ground and 8 km of altitude at Suva.

ACPD
7, 4857–4888, 2007

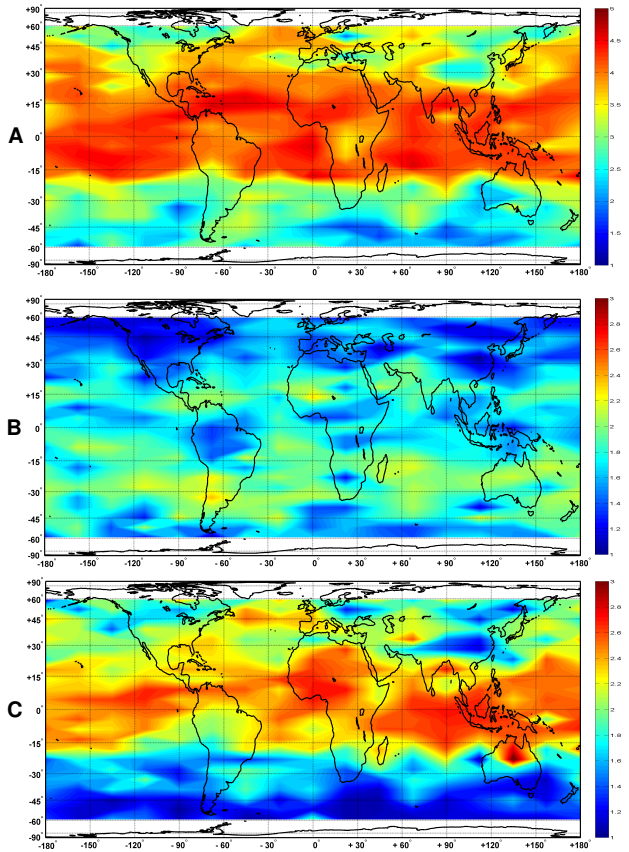

Fig. 5. Global distribution of the DOFS. From top to bottom, $H_2^{16}O$ **(a)**, $H_2^{18}O$ **(b)** and HOD **(c)**, averaged on a 10°×5° longitude-latitude grid, for the 1–10 April 1997 period.

ACPD
7, 4857–4888, 2007

EGU

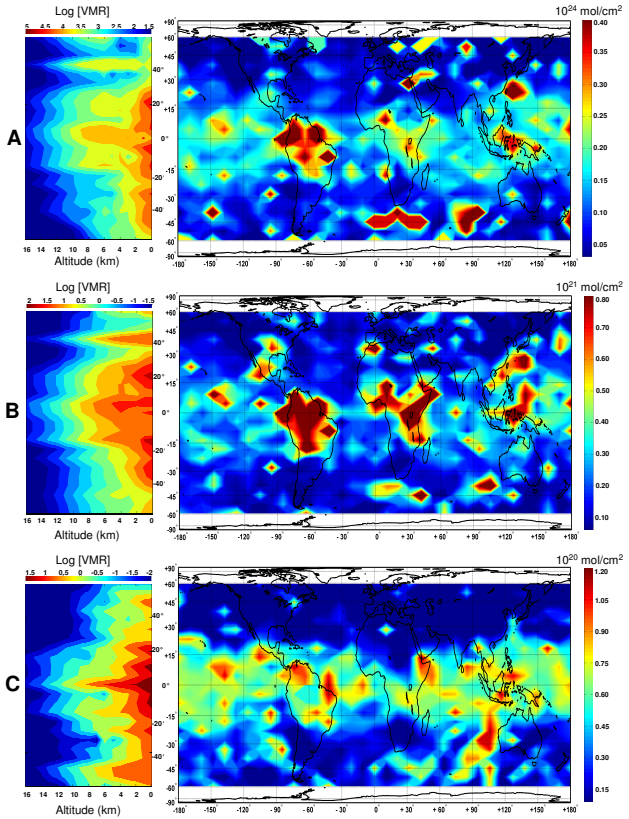

Fig. 6. Global distribution of water vapour isotopologues. Latitudinal distributions (left) and zonal distributions (right) of each isotopologue between 0 and 16 km of altitude. The $H_2^{16}O$ **(a)**, $H_2^{18}O$ **(b)** and HOD **(C)** tropospheric columns (0–16 km) are in 10^{24}, 10^{21} and 10^{20} molecules.cm^{-2}, respectively. Only profiles with a DOFS larger than 1 are considered. Data are averaged on a 10°×5° longitude-latitude grid, for the 1–10 April 1997 period.

ACPD
7, 4857–4888, 2007

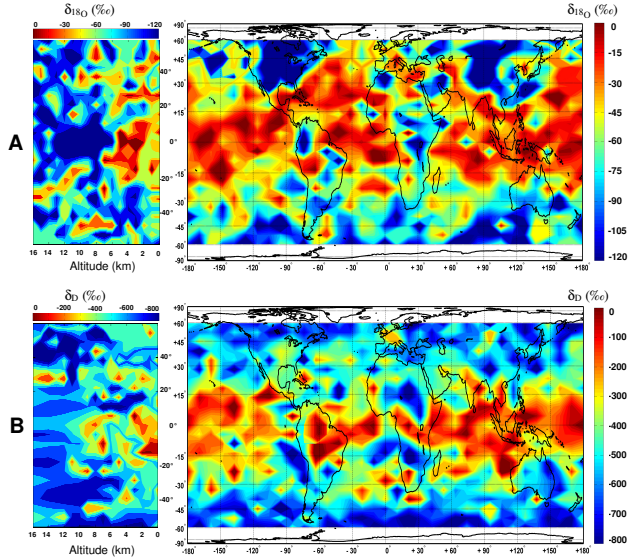

Fig. 7. Global distribution of isotopologic ratios. Latitudinal distributions (left) and zonal distributions (right) of $\delta^{18}O$ **(a)** and δD **(b)** between 2 and 16 km of altitude. Data are averaged on a $10^{\circ} \times 5^{\circ}$ longitude-latitude grid, for the 1–10 April 1997 period.

ACPD
7, 4857–4888, 2007

EGU